Desalination and Water Treatment
www.deswater.com

doi: 10.5004/dwt.2017.20939

86 (2017) 102–114
August

Visible-light-driven photodegradation of aqueous organic pollutants by Ag/AgCl@$Zn_3V_2O_8$ nanocomposites

Mingxiang Hu[a], Xinwei Wang[a], Huanhuan Liu[a], Nanhui Li[a], Tao Li[b], Rui Zhang[a], Deliang Chen[a,b,*]

[a]*School of Materials Science and Engineering, Zhengzhou University, Zhengzhou 450001, China, Tel. +86 371 67781046; Fax: +86 371 67781590; emails: frankhu1993@163.com (M. Hu), 13673973650@126.com (X. Wang), 1099025775@qq.com (H. Liu)*
[b]*School of Chemical Engineering and Energy Technology, Dongguan University of Technology, Dongguan 523808, China, Tel./Fax: +86 76922862039; emails: dlchen@zzu.edu.cn, dlchennano@qq.com (D. Chen)*

Received 29 August 2016; Accepted 12 May 2017

ABSTRACT

This paper reported the synthesis of $Zn_3V_2O_8$ nanoplates and Ag/AgCl@$Zn_3V_2O_8$ nanocomposites, and their visible-light photodegradation of organic pollutants. Ag/AgCl@$Zn_3V_2O_8$ nanocomposites were synthesized via a novel in situ growth of Ag/AgCl nanocrystals on the surfaces of $Zn_3V_2O_8$ nanoplates. The samples of $Zn_3(OH)_2V_2O_7 \cdot 2H_2O$, $Zn_3V_2O_8$ and Ag/AgCl@$Zn_3V_2O_8$ were characterized by the techniques of scanning electron microscope, transmission electron microscopy, X-ray diffraction, X-ray photoelectron spectroscopy, Fourier transform infrared, photoluminescence and UV–vis absorption. The Ag/AgCl@$Zn_3V_2O_8$ nanocomposites showed highly enhanced properties in photodegradating rhodamine B (RhB) and isopropanol under visible-light irradiation (λ > 420 nm), compared with the $Zn_3V_2O_8$ nanoplates. The molar ratios of Ag to Zn and processing parameters have an key effect on their photocatalytic properties. The control experiments with various scavengers indicated that photogenerated electrons (•OH and $\bullet O_2^-$) and holes (h^+) are the major active radicals in the photodegradation of organic species. The synergistic effects of Ag/AgCl and $Zn_3V_2O_8$ in compositions and microstructures account for their enhanced photocatalytic performance. The strategy developed in this work provides an alternative way to design high-performance visible-light-driven photocatalysts with applications in environmental purification.

Keywords: Photodegradation; Organic pollutants; Ag/AgCl@$Zn_3V_2O_8$ photocatalyst

1. Introduction

Photocatalytic degradation of aqueous organic pollutants (e.g., dyes and volatile organic compounds) is a potential strategy to clear sewage [1,2]. TiO_2-based photocatalysts have been widely applied in environmental purification for their long-term stability, high activation and low toxicity [3,4]. However, their large band gaps of larger than 3.2 eV limit their utilization in visible-light photodegradation of pollutants. Therefore, multiple methods have been developed to enhance their photocatalytic properties under visible-light irradiation [5–9]. Some other metal oxide semiconductor-based photocatalysts, like ZnO, $InVO_4$ and Bi_2WO_6, also suffer from similar drawbacks of poor visible-light absorption or low quantum efficiency [10–12]. To design efficient, easy accessible and visible-light-driven photocatalysts is of practical significance and faces big challenges.

Plasmonic photocatalysts, benefited from the localized surface plasmon resonance (SPR) effect of metal nanoparticles (e.g., Au, Ag, Pt and Cu) [13,14], have attracted increasing attention due to their extended absorption of visible light [15,16]. Ag/AgX (X = Cl, Br and I) compounds are efficient active components to design high-performance plasmonic photocatalysts [17–24]. The shape, size and distribution of Ag

* Corresponding author.

nanoparticles in Ag/AgX compounds strongly influence their photocatalytic properties. To minimize the amounts of noble metal, scientists usually immobilize SPR-active metal species on some special substrates to construct hierarchical nanocomposites [25,26] including a series of low-dimensional nanoplates of WO_3 [27], C_3N_4 [27,29], graphene oxide [30], $BiVO_4$ [31], BiOBr [31,32] and $BiOIO_3$ [33].

$Zn_3V_2O_8$ and $Zn_3(OH)_2V_2O_7•2H_2O$ nanostructures with a layered structure are promising materials in designing photocatalysts [34–36]. Flower-like and belt-like $Zn_3(OH)_2V_2O_7•2H_2O$ and $Zn_3V_2O_8$ nanostructures were reported as photocatalysts in photodegradating methylene blue (MB) under visible-light irradiation [35]. Functional modification of $Zn_3V_2O_8$ nanostructures by loading or doping other species is an effective way to improve their photocatalytic performance [36]. However, to the best of our knowledge, there are few reports focused on the $Zn_3V_2O_8$-supported plasmonic photocatalysts. Recently, Ag/AgX (X=Cl, Br) nanocrystals and their nanocomposites have been investigated systematically as visible-light-driven photocatalysts in environmental purification in our previous works [27,37]. In this work, we combine the advantages of $Zn_3V_2O_8$ nanoplates and Ag/AgCl nanocrystals to develop a novel hierarchical photocatalyst of Ag/AgCl@$Zn_3V_2O_8$ nanocomposite (Fig. 1).

2. Experimental section

2.1. Chemicals and reagents

Ammonium metavanadate (NH_4VO_3, Tianjin Guangfu Fine Chemical Industry Research Institute, China), zinc acetate ($C_4H_6O_4Zn•2H_2O$, Tianjin Kermel Chemical Reagent Co., Ltd., China), silver nitrate ($AgNO_3$, Sinopharm Chemical Reagent Co., Ltd., China), sodium chloride (NaCl, Sinopharm Chemical Reagent Co., Ltd.), hexadecyltrimethylammonium bromide (CTAB, Sinopharm Chemical Reagent Co., Ltd.), sodium dodecylbenzenesulfonate (SDBS, Sinopharm Chemical Reagent Co., Ltd.) and polyvinylpyrrolidone (PVP K30, Sinopharm Chemical Reagent Co., Ltd.) were analytically pure. Deionized water was homemade using a water purification system (New Human Power I Scholar, Human Corporation, Beijing, China).

2.2. Synthesis of flower-like $Zn_3(OH)_2V_2O_7•2H_2O$ spheres and $Zn_3V_2O_8$ nanoplates

$Zn_3(OH)_2V_2O_7•2H_2O$ nanocrystals were synthesized via a simple precipitation method. NH_4VO_3 (1 mmol) was dissolved in deionized water (40 mL) at 80°C, and then 10 mL aqueous solution containing $C_4H_6O_4Zn•2H_2O$ (1.5 mmol) was added dropwise into the above solution under magnetic stirring, followed by adding 0.1 g CTAB. The final pH value of the mixture was adjusted to ~9 by adding aqueous ammonia solution. After a continuous stirring for 2 h at 80°C, the above suspension was collected by centrifugation, rinsed with deionized water and finally freeze-dried (FD8-3, SIM International Group Limited Corporation, Hongkong, China). For comparison purpose, similar $Zn_3(OH)_2V_2O_7•2H_2O$ samples were synthesized by replacing CTAB with SDBS and PVP, respectively. $Zn_3V_2O_8$ nanoplates was synthesized by calcined the $Zn_3(OH)_2V_2O_7•2H_2O$ sample obtained with CTAB in a muffle furnace at 300°C–450°C for 2 h.

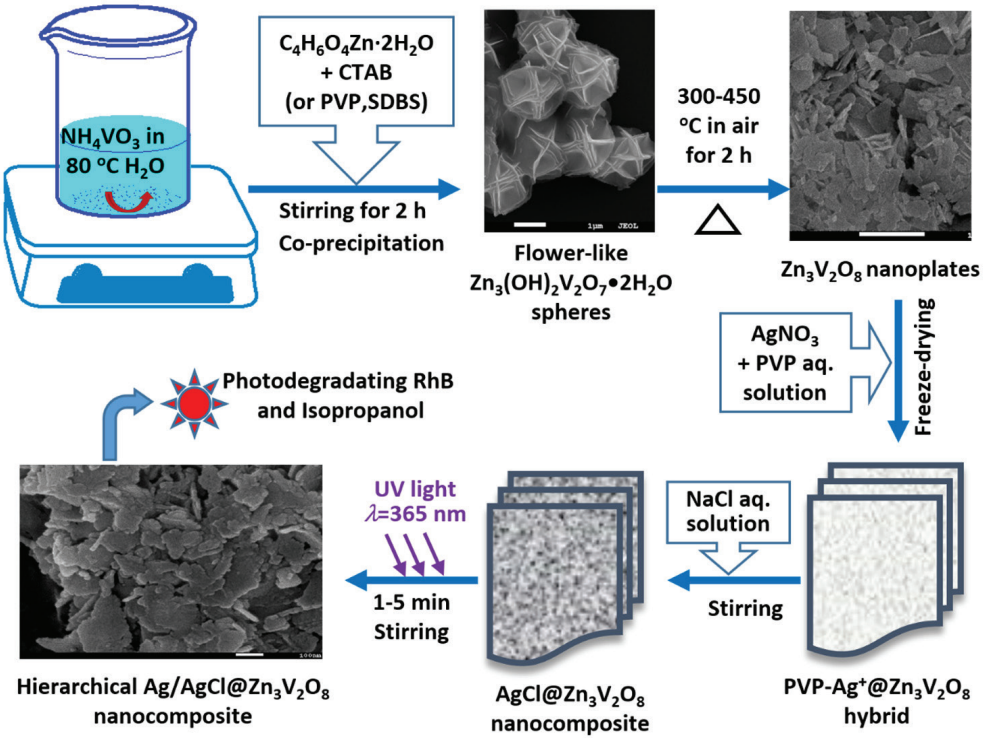

Fig. 1. Schematic illustration of the synthesis of hierarchical Ag/AgCl@$Zn_3V_2O_8$ nanocomposites.

2.3. Synthesis of Ag/AgCl@$Zn_3V_2O_8$ and Ag/AgCl photocatalysts

Essentially, Ag/AgCl@$Zn_3V_2O_8$ nanocomposites were synthesized via a two-step process (Fig. 1). Typically, $Zn_3V_2O_8$ nanoplates (200 mg) and 0.111 g PVP (~1 mmol of units) were dispersed in deionized water (30 mL), and then 1.0 mmol $AgNO_3$ was added into the above mixture, followed by a constant stirring for 45 min. The suspension obtained was freeze-dried to form a hybrid solid of PVP–Ag^+@$Zn_3V_2O_8$. A NaCl aqueous solution (30 mL, 0.5 mmol Cl^-) was then added into the above solid under a magnetic stirring for 1 h in dark. The milky suspension obtained was then irradiated with a UV lamp (λ = 365 nm) for a given time (0-5 min). The solids were collected, rinsed with deionized water and then freeze-dried. The as-obtained samples were Ag/AgCl@$Zn_3V_2O_8$ nanocomposites. For the purpose of comparison, Ag/AgCl@$Zn_3V_2O_8$ nanocomposites with various molar ratios of Ag to Zn were synthesized with different processing parameters. The Ag/AgCl@$Zn_3V_2O_8$ samples obtained were denoted as "$T_xM_yt_z$", where T_x means that the calcination temperature of $Zn_3(OH)_2V_2O_7$•$2H_2O$ is x °C, M_y means that the molar ratio of Ag to Zn is y%, and t_z means that the UV-photoreduction time is z min. Some parameters used in the synthesis of Ag/AgCl@$Zn_3V_2O_8$ samples were listed in Table 1. It should be noted that the Ag-to-Zn ratio is controlled by the amounts of their precursors added.

For comparison purpose, the Ag/AgCl sample was also synthesized via a similar two-step method. Typically, $AgNO_3$ (1 mmol) and PVP (1 mmol unit) were dissolved in 30 mL water, and the above mixture was kept stirring for 1 h at room temperature before freeze-drying. Then, 10 mL of NaCl aqueous solution containing 0.5 mmol of Cl^- was added to the above Ag^+–PVP solid and kept magnetic stirring for another 1 h to form AgCl nanocrystals, which were then irradiated by a UV lamp (λ = 365 nm) for 1 min to partly reduce Ag^+ ions to form a Ag/AgCl nanocomposite (S5 in Table 1).

2.4. Characterization of composition and morphology

The phases were determined by X-ray diffraction (XRD, Beijing Purkinje General Instrument Co. Ltd., China) using a Cu Kα radiation (λ = 1.5406 Å) with a tube voltage of 36 kV and a current of 20 mA (scanning rate: ~4°/min in a 2q range of 20°–70°). The morphologies were observed by a field emission scanning electron microscope (FESEM, JEOL, JSM-7001F, Japan). Before SEM observation, the samples were coated with a thin Pt film using a coater (JEOL, JFC-1600, Japan) under 20 mA for 50 s. The UV–vis diffuse reflectance (DR) spectra were performed on a UV–vis–NIR spectrophotometer (Shimadzu, UV-3600) in a wavelength range of 240–800 nm. The X-ray photoelectron spectroscopy (XPS) spectra were recorded on a multi-purpose X-ray photoelectron spectroscope (Sigma Probe, Thermo VG Scientific, Waltham, MA, USA) with a microfocused monochromatic X-ray source (Al Ka), using adventitious carbon (C 1s, 284.6 eV) as the calibration reference. Fourier transform infrared (FTIR) spectra were recorded on a Nicolet 460 spectrophotometer using the KBr disk technique. The N_2 adsorption–desorption isothermal analysis was performed on a gas adsorption analyzer (BELSORP-miniII, Microtrac BEL, Inc., Japan). Transmission electron microscopy (TEM) images were obtained using a JEOL JEM-2100 microscope, with an accelerating voltage of 200 kV. The photoluminescence (PL) spectrum of Ag/AgCl@$Zn_3V_2O_8$ was detected using a spectrofluorometer (FluoroMax-4, HORIBA JobinYvon, France) at room temperature, and a 3D-PL spectrum was used to determine whether the sample has a PL effect or not in a wavelength of 400–800 nm.

2.5. Test of photocatalytic property

Photocatalytic properties of the Ag/AgCl@$Zn_3V_2O_8$ samples were tested by photocatalytically degradating organic pollutants, for example, rhodamine B (RhB) and isopropanol, under the artificial visible light provided by a 300 W Xe lamp

Table 1
Summary of processing parameters and RhB photodegradation rate constants of Ag/AgCl@$Zn_3V_2O_8$ photocatalysts

Sample	AgCl, mmol	$Zn_3V_2O_8$, mmol	Molar ratio $R_{Ag/Zn}$	Calcination temperature (T), °C	Photoreduction time (t), min	k, min^{-1}
S1 ($T_{300}M_{35}t_2$)	0.5	0.47	~0.35	300	2.0	0.111
S2 ($T_{350}M_{35}t_2$)	0.5	0.47	~0.35	350	2.0	0.125
S3 ($T_{400}M_{35}t_2$)	0.5	0.47	~0.35	400	2.0	0.195
S4 ($T_{450}M_{35}t_2$)	0.5	0.47	~0.35	450	2.0	0.136
S5 (t1)	0.5	0.00	–	–	1.0	0.110
S6 ($T_{400}M_{141}t_2$)	0.5	0.12	~1.41	400	2.0	0.059
S7 ($T_{400}M_{71}t_2$)	0.5	0.24	~0.71	400	2.0	0.081
S8 ($T_{400}M_{23}t_2$)	0.5	0.71	~0.23	400	2.0	0.203
S9 ($T_{400}M_{18}t_2$)	0.5	0.94	~0.18	400	2.0	0.080
S10 ($T_{400}M_{23}t_0$)	0.5	0.71	~0.23	400	0.0	0.018
S11 ($T_{400}M_{23}t_{0.5}$)	0.5	0.71	~0.23	400	0.5	0.122
S12 ($T_{400}M_{23}t_1$)	0.5	0.71	~0.23	400	1.0	0.282
S13 ($T_{400}M_{23}t_3$)	0.5	0.71	0.23	400	3.0	0.157
S14 ($T_{400}M_{23}t_5$)	0.5	0.71	~0.23	400	5.0	0.037
S15 ($T_{400}M_0t_0$)	0	0.71	0	400	0.0	0.008

(NBeT, HSX-F300) equipped with an ultraviolet cutoff filter ($\lambda \geq 420$ nm). The light density (about 100 mW/cm^2) was controlled by adjusting the distance between the lamp and the surface of the photodegradation solution, measured using a light meter (Tenmars TM-208, USA).

All the photocatalytic tests were conducted under ambient conditions with a photocatalyst concentration of 1 g/L. Typically, 50 mg of Ag/AgCl@$Zn_3V_2O_8$ sample was first dispersed in a 100 mL beaker containing 45 mL of water under magnetic stirring, followed by a sonication treatment for 3 min. Second, the above suspension was moved to a dark condition, and 5 mL of 100 mg/L RhB aqueous solution was carefully added. The dye-containing suspension was kept magnetically stirring in dark for 30 min to reach a dye-adsorption equilibrium on the surfaces of photocatalysts. The suspension with photocatalysts and dye molecules was then exposed to visible light. Aliquots of solutions (3–5 mL) were drawn from the reaction system using a syringe at a given degradation duration. The suspensions sampled were centrifuged at 7,000 rpm (rotation per minute) for 6 min to remove the solid photocatalyst particles completely, and the upper clear solutions were then transferred to a quartz cuvette to measure their absorption spectra in a wavelength range of 300–800 nm using a UV–vis spectrophotometer (UV-1800PC, Mapada Instruments, China). The concentration ratios (C/C_0) of the dye solutions were determined by the absorbance (A/A_0) at a certain wavelength (i.e., 551 nm for RhB), according to the relationship of $C = k'A$. Here, k' is a constant, A is the absorbance of the dye solution at time t, and A_0 is the absorbance at the beginning of the visible-light irradiation; C is the concentration of the dye aqueous solution at time t, and C_0 is the concentration at the beginning of the visible-light irradiation. If the photodegradation reaction follows the first-order kinetics, that is, $\ln(A/A_0) = \ln(C/C_0) = -kt$, the photodegradation rate constant (k/min^{-1}) can be determined by the $\ln(A/A_0) - t$ plots [37].

Isopropanol, without any absorption in the visible-light range, was also used as the target pollutant to evaluate the photocatalytic activity of Ag/AgCl@$Zn_3V_2O_8$ sample. The amounts of the residual organic substances after various photodegradation times were estimated by the chemical oxygen demand (COD), measured according to the standard method of potassium dichromate titration (GB 11914-89).

3. Results and discussion

3.1. Synthesis and characterization

The XRD patterns of the $Zn_3(OH)_2V_2O_7 \bullet 2H_2O$ samples with different surfactants (i.e., PVP, CTAB or SDBS) are shown in Fig. 2. All of the peaks can be readily indexed to the hexagonal $Zn_3(OH)_2V_2O_7 \bullet 2H_2O$ phase according to JCPDS card no. 87-0417 [39], indicating that the samples consist of a pure $Zn_3(OH)_2V_2O_7 \bullet 2H_2O$ phase. The possible chemical reaction describing the formation of $Zn_3(OH)_2V_2O_7 \bullet 2H_2O$ can be expressed as Eq. (1).

$$2VO_3^- + 3Zn^{2+} + 4OH^- + H_2O \xrightarrow{80°C,\ pH=9,\ surfactants} Zn_3(OH)_2V_2O_7 \cdot 2H_2O \quad (1)$$

The morphology of the precursors was observed by SEM. Fig. 3 shows the typical FESEM images of the $Zn_3(OH)_2V_2O_7 \bullet 2H_2O$ samples obtained via the precipitation reaction with different surfactants ((a)–(c) CTAB, (d)–(f) PVP and (g)–(i) SDBS) and without surfactant (j)–(l). The $Zn_3(OH)_2V_2O_7 \bullet 2H_2O$ samples show a similar morphology of flower-like spheres with an apparent diameter of 1–2 μm.

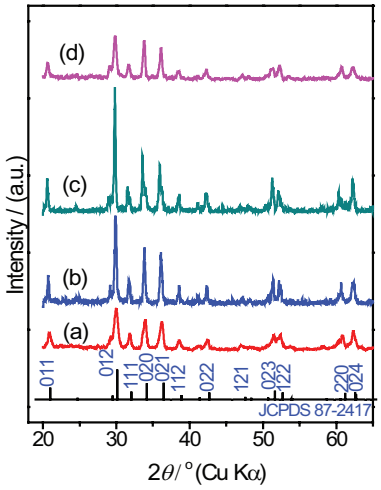

Fig. 2. Powder XRD patterns of $Zn_3(OH)_2V_2O_7 \bullet 2H_2O$ nanocrystals obtained with various surfactants: (a) CTAB, (b) PVP and (c) SDBS and without any surfactant (d).

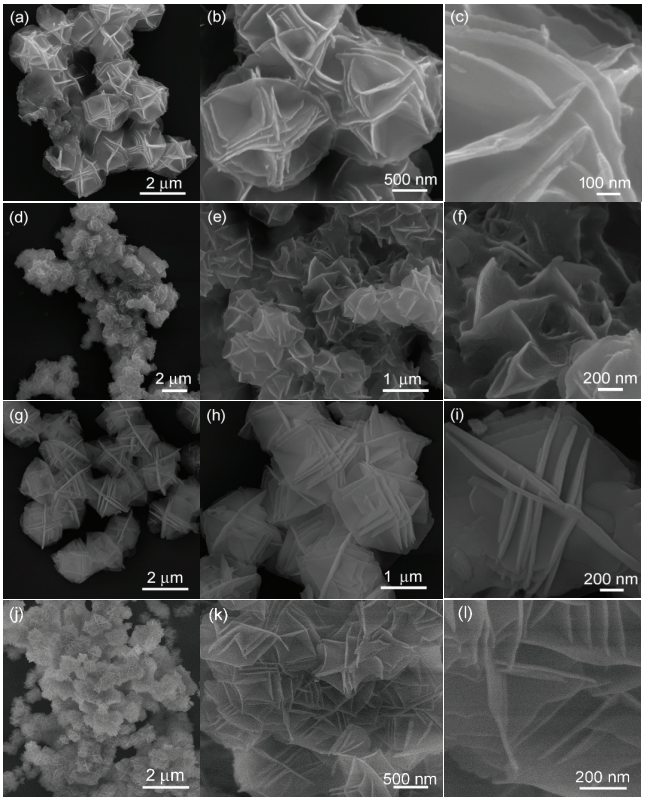

Fig. 3. FESEM images of $Zn_3(OH)_2V_2O_7 \bullet 2H_2O$ nanocrystals obtained with various surfactants: (a)–(c) CTAB, (d)–(f) PVP and (g)–(i) SDBS and without any surfactant (j)–(l).

Figs. 2(c), (f), (i) and (l) suggest that the flower-like spheres are formed by assembling the pristine nanoplates with a nanoscale thickness (ca. 10–20 nm).

The pore structures of the samples were estimated by the N_2 adsorption–desorption test. Fig. 4(a) shows the typical nitrogen adsorption–desorption isotherms of the $Zn_3(OH)_2V_2O_7 \cdot 2H_2O$ samples obtained with CTAB (A) or not (B). Both the isotherms are of a type IV characteristic, and the high adsorption at the relatively high pressure (P/P_0) range (approaching 1.0) suggests the existence of mesopores (2–50 nm) and macropores (>50 nm) in the $Zn_3(OH)_2V_2O_7 \cdot 2H_2O$ samples [39]. The shapes of the hysteresis loops are of a type H3 feature, which associates with aggregates of plate-like particles and slit-like pores [39,40]. The mesopores and macropores are mainly caused by the house-of-card structure formed by the aggregated flower-like spheres. The specific surface area of the $Zn_3(OH)_2V_2O_7 \cdot 2H_2O$ sample obtained with CTAB is 29.3 m^2/g, larger than that (14.8 m^2/g) of the one obtained without CTAB. The N_2 adsorption–desorption and pore-size distribution curves of the Ag/AgCl@$Zn_3V_2O_8$ sample are shown in Fig. 4(b). The sample has a specific surface area of 39.3 m^2/g, larger than that (29.3 m^2/g) of its precursor of $Zn_3(OH)_2V_2O_7 \cdot 2H_2O$. The enhanced surface area can provide more active sites for catalytic applications. The inset in Fig. 4(b) shows the pore-size distribution curve, indicating that the sample is of a large pore distribution range.

$$Zn_3(OH)_2V_2O_7 \cdot 2H_2O \xrightarrow{300-450^\circ C,\ \text{in air}} Zn_3V_2O_8 + 3H_2O \quad (2)$$

$$Zn_3V_2O_8 + Ag^+ + PVP \xrightarrow{\text{Vacuum freeze-drying}} PVP\text{-}Ag^+@Zn_3V_2O_8 \quad (3)$$

$$PVP\text{-}Ag^+@Zn_3V_2O_8 + Cl^- \xrightarrow{\text{UV irradiation and washing}} Ag/AgCl@Zn_3V_2O_8 \quad (4)$$

The $Zn_3V_2O_8$ phase was formed by removing the constitutional and crystal water molecules of the $Zn_3(OH)_2V_2O_7 \cdot 2H_2O$ sample, which was calcined at 300°C–450°C in air (Eq. (2)). The as-obtained $Zn_3V_2O_8$ nanocrystals were used as the substrate to construct Ag/AgCl@$Zn_3V_2O_8$ nanocomposites. The formation of Ag/AgCl@$Zn_3V_2O_8$ nanocomposite can be expressed using Eqs. (3) and (4), involving the adsorption of Ag^+ ions and growth of AgCl nanoparticles on the $Zn_3V_2O_8$ surfaces. Finally, the UV-light photoreduction of AgCl species leads to the formation of Ag/AgCl@$Zn_3V_2O_8$ nanocomposites. As Figs. 3 and 4 show, various surfactants have little effect on the microstructure of $Zn_3(OH)_2V_2O_7 \cdot 2H_2O$ samples. For the sake of simplicity, we chose the $Zn_3(OH)_2V_2O_7 \cdot 2H_2O$ sample obtained with CTAB as the model precursor to prepare Ag/AgCl@$Zn_3V_2O_8$ nanocomposites.

Fig. 5 compares the XRD patterns of the $Zn_3(OH)_2V_2O_7 \cdot 2H_2O$ nanocrystals, $Zn_3V_2O_8$ nanoplates obtained by calcining $Zn_3(OH)_2V_2O_7 \cdot 2H_2O$ at 400°C, and the as-obtained Ag/AgCl@$Zn_3V_2O_8$ nanocomposites (S12 in Table 1). The $Zn_3(OH)_2V_2O_7 \cdot 2H_2O$ phase (Fig. 5(a)) is transformed to a pure $Zn_3V_2O_8$ phase (Fig. 5(b)) by calcining it at 400°C for 2 h. Three strong peaks at 34.9°, 43.1° and 62.9° can be indexed to the (122), (042) and (442) reflections of the $Zn_3V_2O_8$ phase, respectively, according to the JCPDS

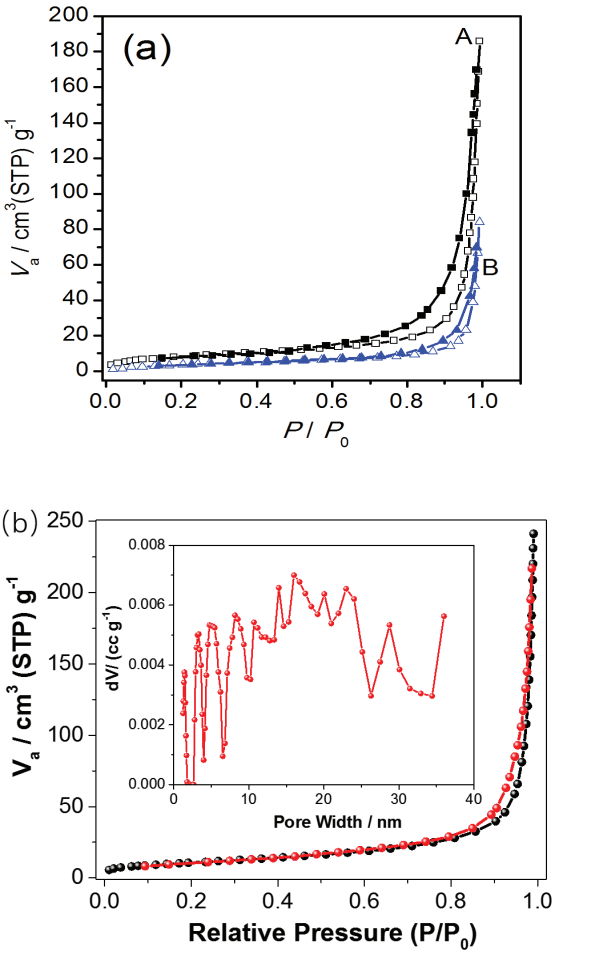

Fig. 4. Nitrogen adsorption–desorption isotherms (solid: adsorption; open: desorption) of (a) $Zn_3(OH)_2V_2O_7 \cdot 2H_2O$ nanocrystals obtained with CTAB (A) and without CATB (B), and (b) Ag/AgCl@$Zn_3V_2O_8$ nanocomposite (inset: pore-size distribution).

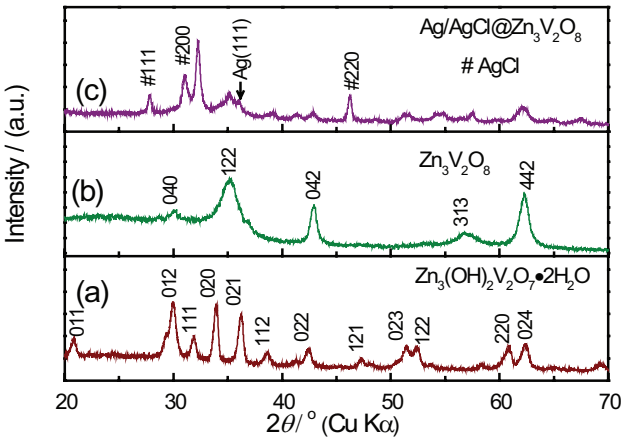

Fig. 5. XRD patterns of (a) $Zn_3(OH)_2V_2O_7 \cdot 2H_2O$ nanocrystals synthesized with CTAB, (b) $Zn_3V_2O_8$ nanoplates (S14) obtained by calcining $Zn_3(OH)_2V_2O_7 \cdot 2H_2O$ at 400°C and (c) Ag/AgCl@$Zn_3V_2O_8$ nanocomposites (S12).

card no. 34-0378 (space group: *Abam* [64]; cell parameters: a = 0.8299 nm, b = 1.152 nm, c = 0.6111 nm) [35,36]. The broadening of the XRD peaks suggests that the $Zn_3V_2O_8$ sample is of small crystal grains. Fig. 5(c) shows a typical XRD pattern of the Ag/AgCl@$Zn_3V_2O_8$ nanocomposite (S12 in Table 1). These peaks at 2q = 27.8°, 32.2° and 46.3° can be indexed to the (111), (200) and (220) reflections of the AgCl phase, respectively, according to the JCPDS card no. 31-1238 (space group: *Fm*3*m* [225]) [37,38], and the other peaks belong to the $Zn_3V_2O_8$ phase [36]. The XRD pattern of the Ag/AgCl@$Zn_3V_2O_8$ sample can be seen as a superimposition of those XRD patterns of $Zn_3V_2O_8$ and AgCl phases. The weak peak at ~37° (Fig. 5(c)) can be assigned to the (111) reflection of metal Ag species [27,37].

Fig. 6 shows the typical FESEM images of the $Zn_3V_2O_8$ (S15 in Table 1) and Ag/AgCl@$Zn_3V_2O_8$ (S12 in Table 1) samples. As Figs. 6(a) and (b) show, the $Zn_3V_2O_8$ sample obtained by calcining flower-like $Zn_3(OH)_2V_2O_7 \bullet 2H_2O$ spheres (Figs. 2(a)–(c)) consists of $Zn_3V_2O_8$ nanoplates with a thickness of several nanometers. Figs. 6(c) and (d) show the typical FESEM images of the Ag/AgCl@$Zn_3V_2O_8$ sample, and one can find that small Ag/AgCl nanoparticles (5–10 nm in size) are attached on the surfaces of $Zn_3V_2O_8$ nanoplates uniformly.

To further understand the formation of AgCl@$Zn_3V_2O_8$ nanocomposites, we used FTIR spectra (Fig. 7) to characterize the PVP–Ag^+@$Zn_3V_2O_8$, PVP and $Zn_3V_2O_8$ samples. The wide absorption band at ~3,445 cm^{-1} exists in the three samples, belonging to the stretching vibration mode of the –OH groups in the water molecules absorbed. The bands at 2,960 and 2,860 cm^{-1} correspond to the asymmetric CH_2 stretching and symmetric CH_2 stretching of PVP, respectively. The bands at ~1,643 cm^{-1} correspond to the stretching vibration region of C=O, the bands at 1,020–1,230 cm^{-1} belong to the stretching vibration region of C-N, and the bands at 1,050–1,250 cm^{-1} are due to the stretching vibration region of the C–O group. The absorption bands at ~801 and ~931 cm^{-1} can be attributed to the V–O vibration [46]. The band at ~1,385 cm^{-1} only occurs in the hybrid of PVP–Ag^+@$Zn_3V_2O_8$, indicating the formation of an organic–inorganic hybrid [37]. Such interaction between Ag^+ and functional groups of PVP molecules surrounding the surfaces of $Zn_3V_2O_8$ nanoplates is favorable in forming Ag/AgCl@$Zn_3V_2O_8$ nanocomposites.

Fig. 8 shows the typical XPS spectra of Ag/AgCl@$Zn_3V_2O_8$ nanocomposite (S12 in Table 1). The wide survey scan spectrum (Fig. 8(a)) indicates that the sample consists of elements of Zn, Cl, C, Ag and O. Figs. 7(b) and (c) show the core-level XPS spectra of Zn 2p and V 2p, respectively. Their binding energies are similar to those of ZnO and V_2O_5. Fig. 8(d) shows the core-level XPS spectrum of Ag 3d, which can be subdivided into two sets of XPS spectra, including four peaks: 367, 368, 373 and 374 eV. The two strong peaks at 367 and 373 eV are attributed to Ag^+ species of the AgCl solid, belonging to the binding energies of Ag $3d_{5/2}$ and Ag $3d_{3/2}$, respectively. The peaks at 368 and 374 eV can be attributed to metal Ag^0 species [27,28]. The two peaks at 197.6 and 199.2 eV belong to Cl $2p_{1/2}$ and $2p_{3/2}$, respectively, confirming the existence of AgCl [37]. Taking the SEM, XRD and XPS results into account, the Ag/AgCl@$Zn_3V_2O_8$ sample (S12) consists of metal Ag, AgCl and $Zn_3V_2O_8$, and the Ag/AgCl species in the

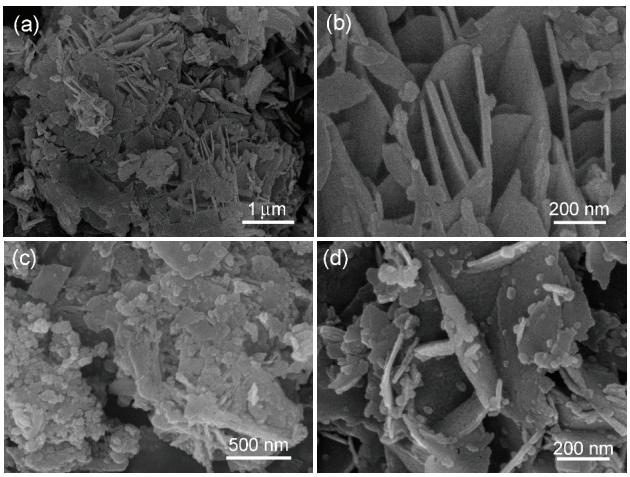

Fig. 6. FESEM images of (a)–(b) $Zn_3V_2O_8$ nanosheets (S15) and (c)–(d) Ag/AgCl@$Zn_3V_2O_8$ nanocomposite (S12).

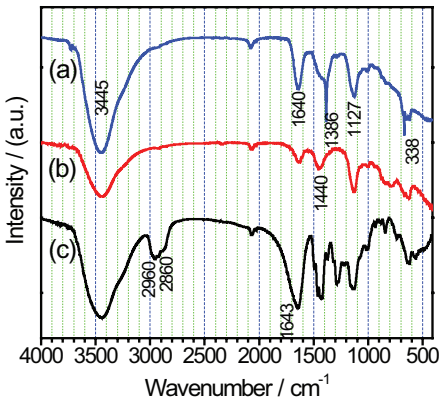

Fig. 7. FTIR spectra of (a) PVP–Ag^+@$Zn_3V_2O_8$ hybrid, (b) $Zn_3V_2O_8$ nanocrystals and (c) pure PVP.

Ag/AgCl@$Zn_3V_2O_8$ composite have a small particle size less than 20 nm.

Fig. 9 shows the typical TEM images and corresponding energy dispersive spectroscopy (EDS) spectrum of the as-obtained Ag/AgCl@$Zn_3V_2O_8$ sample. The low-magnification images in Figs. 9(a) and (c) show that the Ag/AgCl nanoparticles with a size range of 30–50 nm are attached on the surfaces of the $Zn_3V_2O_8$ nanoplates. Fig. 9(b) shows a high-resolution TEM (HRTEM) image, in which two Ag/AgCl nanoparticles can be seen clearly. The crystal lattices of the edges in the Ag/AgCl nanoparticles can be recognized, and the interplanar distance can be measured to be ~0.243 nm, which is close to the interplanar distance (0.231 nm) of the Ag (111) plane. Fig. 9(d) shows that the Ag/AgCl nanoparticles are well distributed separately on the $Zn_3V_2O_8$ nanoplate. The enlarged part in Fig. 9(e) indicates that the Ag nanoparticles are embedded in the AgCl particles and the $Zn_3V_2O_8$ nanoplates support the Ag/AgCl nanoparticles. Fig. 9(f) shows the corresponding EDS spectrum. The elements of Zn, V, Ag, Cl and O come from the Ag/AgCl@$Zn_3V_2O_8$ sample, and the C and Cu elements should be due to the Cu grid with a carbon film.

3.2. Photodegradation performance and possible photocatalytic mechanisms of Ag/AgCl@$Zn_3V_2O_8$ nanocomposites

The photocatalytic performance of the Ag/AgCl@$Zn_3V_2O_8$ nanocomposites was evaluated by photodegradating RhB and isopropanol under visible-light irradiation (λ > 420 nm) according to the method reported previously [37]. To quantify their photocatalytic activity, we calculated the rate constants (k, min^{-1}) according to the first-order reaction kinetics, and listed them in Table 1.

Fig. 10 shows the typical photocatalytic properties of the Ag/AgCl@$Zn_3V_2O_8$ sample (S12), compared with the Ag/AgCl and $Zn_3V_2O_8$ samples. Fig. 10(a) shows the UV–vis absorption spectra of the RhB aqueous solutions after visible-light irradiation with various times (0–18 min) using Ag/AgCl@$Zn_3V_2O_8$ (S12) as the photocatalyst. One can see that RhB can be photodegradated almost completely in 18 min. Comparatively, Fig. 10(b) shows the UV–vis absorption spectra of the RhB aqueous solutions after visible-light-driven photodegradation with various times using Ag/AgCl as the photocatalyst. The RhB solution is partly photodegradated even after a

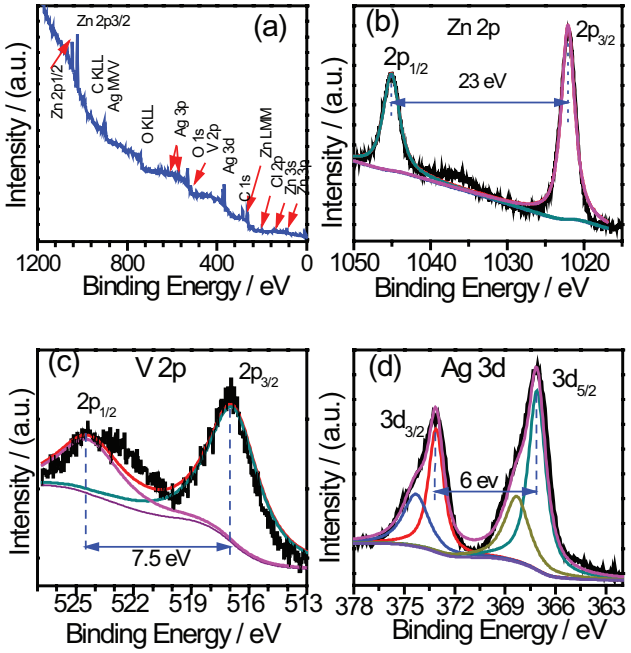

Fig. 8. XPS spectra of the Ag/AgCl@$Zn_3V_2O_8$ (S12) photocatalyst: (a) a wide survey scan, and (b)–(d) core-level spectra of: (b) Zn 2p, (c) V 2p and (d) Ag 3d.

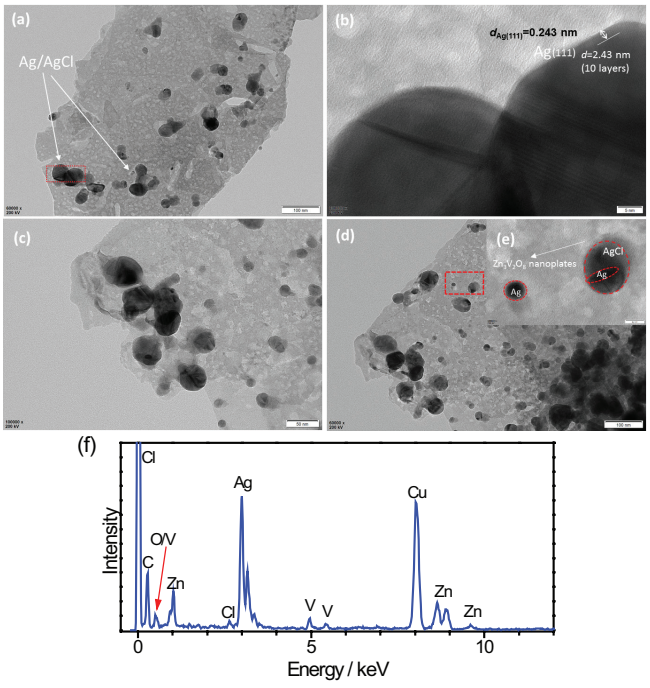

Fig. 9. TEM observations of the Ag/AgCl@$Zn_3V_2O_8$ (S12) nanocomposite: (a)–(e) TEM images and (f) EDS spectrum.

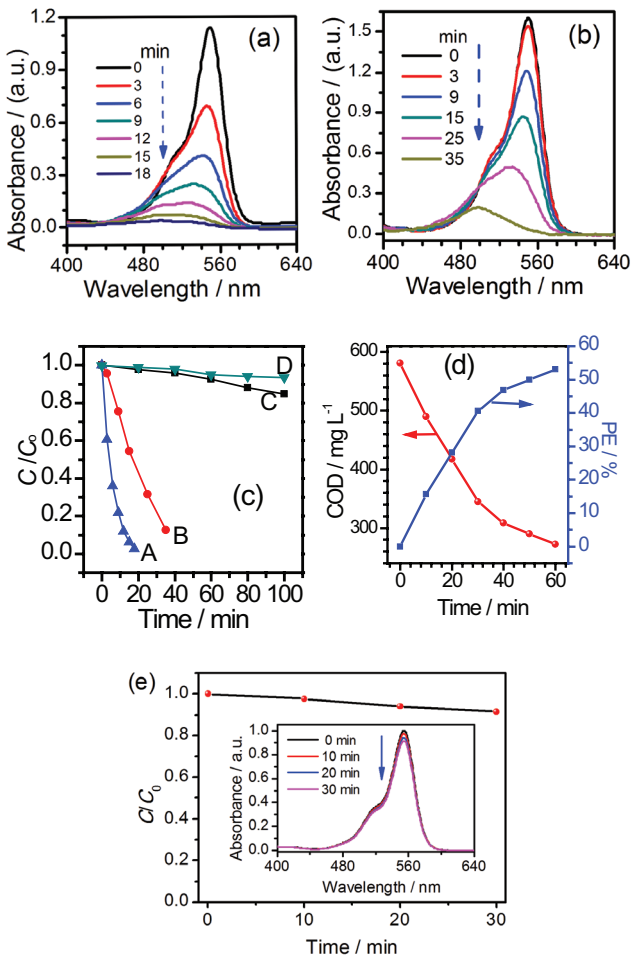

Fig. 10. (a)–(b) UV–vis absorption spectra of the RhB aqueous solutions after visible-light-driven photodegradation using (a) Ag/AgCl@$Zn_3V_2O_8$ (S12) and (b) Ag/AgCl (S5) as the photocatalysts. (c) Photocatalytic RhB degradation curves with (A) Ag/AgCl@$Zn_3V_2O_8$ (S12), (B) Ag/AgCl (S5), (C) $Zn_3V_2O_8$ (S15) and (D) P25 (TiO_2) under visible-light irradiation. (d) The COD curve and photocatalytic efficiency of isopropanol photodecomposed by Ag/AgCl@$Zn_2V_2O_8$ (S12) nanocrystals under visible-light irradiation. (e) Adsorption of RhB on the Ag/AgCl@$Zn_3V_2O_8$ (S12) catalyst in dark (the inset is the UV–vis absorption spectra).

reaction of 35 min. Also, the peak at 498 nm increases as the peak at 551 nm decreases, suggesting that a new intermediate dye is formed with RhB photodegradation. Considering the fast degradation of the Ag/AgCl@$Zn_3V_2O_8$ sample (S12), the influence of the self-degradation of RhB can be neglected. The previous report [42] shows that there is only a 1.5% self-degradation of RhB irradiated under visible light for 120 min.

Fig. 10(c) shows the photocatalytic degradation (C/C_0) of RhB vs. the irradiation time using Ag/AgCl@$Zn_3V_2O_8$ (A), Ag/AgCl (B) and $Zn_3V_2O_8$ (C) as the photocatalysts, respectively. The $Zn_3V_2O_8$ sample shows the lowest photocatalytic rate constant (k = 0.008 min^{-1}), while the Ag/AgCl@$Zn_3V_2O_8$ sample has the highest photocatalytic rate constant (k = 0.282 min^{-1}). For the RhB photodegradation with the Ag/AgCl@$Zn_3V_2O_8$ sample, there is almost no obvious blue shift. The $Zn_3V_2O_8$ nanoplates may play a key role both as a carrier-donor and as a substrate to support the plasmonic photocatalyst of Ag/AgCl nanoparticles. The photocatalytic activity and stability of the photocatalysts are thus greatly enhanced by loading Ag/AgCl particles on the surface of $Zn_3V_2O_8$ nanoplates.

To corroborate the photocatalytic activity without a photosensitive agent, isopropanol was used as the probe substance to evaluate the photocatalytic activity of the Ag/AgCl@$Zn_3V_2O_8$ (S12), because isopropanol has no absorption in the visible-light range. After photocatalytic degradation, the amount of residual isopropanol in the solution was measured by COD. The photodegradation efficiency (PE, %) was calculated according to PE = 100 × ($COD_{initial}$ − COD_{final})/$COD_{initial}$, where $COD_{initial}$ and COD_{final} are the COD data tested at the initial stage without photodegradation and those tested at a given photodegradation time, respectively. Fig. 10(d) shows the photodegradation curve of isopropanol under visible-light irradiation in the presence of Ag/AgCl@$Zn_3V_2O_8$ (S12) as the photocatalyst. The COD value of the isopropanol solution decreases from the initial value of 575–275 mg/L as the photodegradation time increases from 0 to 60 min, and the photodegradation efficiency reaches ~52%. This result confirms that the Ag/AgCl@$Zn_3V_2O_8$ nanocomposite is of a high photocatalytic activity in degradating both organic dyes (i.e., RhB) and alcohols (i.e., isopropanol) under visible-light irradiation.

Adsorption is one of the most important factors that influence the photocatalytic ability. Fig. 10(e) shows the typical adsorption curve of RhB molecules onto the Ag/AgCl@$Zn_3V_2O_8$ catalyst in dark. After an adsorption of 30 min, there is about 10% of RhB molecules adsorbed on the photocatalyst. Compared with the photocatalytic data (Figs. 10(a) and (c)), one can see that the total amount of RhB molecules can be photodegradated within 20 min under visible-light irradiation. Therefore, we can safely conclude that the photocatalytic degradation is the essential factor that results in the reduction of RhB molecules.

To explore the factors that influence the RhB photodegradation activity, we designed a series of control experiments (Fig. 11, S1–S4 in Table 1). Fig. 11(a) shows the effect of the calcination temperature (300°C–450°C) of $Zn_3(OH)_2V_2O_7$•$2H_2O$ on the photocatalytic activity of the Ag/AgCl@$Zn_3V_2O_8$ samples. One can see that the Ag/AgCl@$Zn_3V_2O_8$ photocatalyst (S3 in Table 1) with the 400°C–$Zn_3V_2O_8$

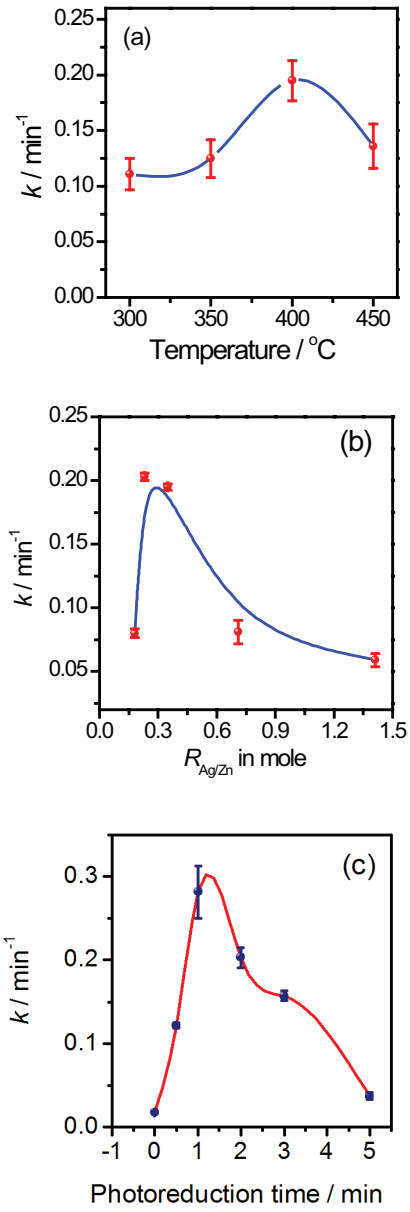

Fig. 11. RhB photodegradation rate constants of the Ag/AgCl@$Zn_3V_2O_8$ photocatalysts under various conditions: (a) various calcining temperatures of $Zn_3V_3O_8$, (b) molar Ag-to-Zn ratios ($R_{Ag/Zn}$) and (c) photoreduction times.

nanoplates shows the highest RhB-photodegradation rate constant (k_{400} = 0.195 min^{-1}), and the rate constant changes with a decreasing order as $k_{400} > k_{450} > k_{350} > k_{300}$. This result can be explained according to the TG–DTA data. The substrate of $Zn_3V_2O_8$ nanoplates obtained at 400°C is of a stable phase with a suitable microstructure, but the lower or higher calcination temperatures damage their compositions or microstructures.

The effect of the Ag-to-Zn ratios on the photocatalytic activity was further investigated. The Ag-to-Zn ratios listed in Table 1 were determined by their amounts added during the synthetic process. Fig. 11(b) shows the effect of the Ag-to-Zn molar ratios ($R_{Ag/Zn}$ = 0.18–1.41) on the photocatalytic activities of the Ag/AgCl@$Zn_3V_2O_8$ nanocomposites

(S6–S9 in Table 1). When $R_{Ag/Zn}$ is about 0.23–0.36, k reaches a peak value of k = 0.203 min^{-1}, and the photocatalysts with a lower or higher $R_{Ag/Zn}$ show a lower photocatalytic activity in photodegradating RhB under the visible-light irradiation. A longer UV-light irradiation time during the photoreduction of Ag^+ ions means to form more metal Ag species, and the photoreduction time is also a critical factor that influences the photocatalytic activity of the Ag/AgCl@$Zn_3V_2O_8$ nanocomposites (Fig. 11(c), S10–S14 in Table 1). As Fig. 11(c) shows, the Ag/AgCl@$Zn_3V_2O_8$ nanocomposite with a photoreduction reaction of 1 min has the highest photocatalytic rate constant (k = 0.282 min^{-1}) in degradating RhB.

The absorbance of visible light is a key factor that influences the photocatalytic performance of a photocatalyst. To understand the photocatalytic behavior of the Ag/AgCl@$Zn_3V_2O_8$ nanocomposites, we first measured the UV–vis DR spectra of these samples and calculated their bandgaps (Fig. 12): (A) Ag/AgCl@$Zn_3V_2O_8$ (S12 in Table 1) with a photoreduction of 1 min, (B) Ag/AgCl@$Zn_3V_2O_8$ (S14 in Table 1) with a photoreduction of 5 min, (C) $Zn_3V_2O_8$, (D) $Zn_3(OH)_2V_2O_7 \bullet 2H_2O$ and (E) TiO_2 (P25). As Fig. 12 shows, $Zn_3(OH)_2V_2O_7 \bullet 2H_2O$ shows almost no absorption in the visible-light region (λ = 420–800 nm), similar to TiO_2 (P25), and its photocatalytic property is inefficient because of its large band gap (~3.34 eV). Using the similar method, the band gap of $Zn_3V_2O_8$ is calculated to be ~3.17 eV, and it can absorb a small amount of visible light. Comparatively, the Ag/AgCl@$Zn_3V_2O_8$ (S12) sample with a photoreduction of 1 min has an apparent bandgap of ~2.13 eV, and shows the highest absorbance in the visible-light region (λ = 420–800 nm) according to its UV–vis DR spectra. The enhancement in visible-light absorption should be due to the hybridization of Ag, AgCl and $Zn_3V_2O_8$. It needs to be noted that a longer photoreduction time weakens its visible-light absorbance, corroborated by the UV–vis DR spectrum of Ag/AgCl@$Zn_3V_2O_8$ sample (S14 in Table 1, bandgap = ~2.99 eV) obtained with a photoreduction time of 5 min. Therefore, we conclude that the improvement of the Ag/AgCl@$Zn_3V_2O_8$ photocatalyst in photodegradating organic pollutants under visible-light irradiation is partly resulted from the enhancement in the visible-light absorbance. A 3D PL spectrum (Fig. 12(c)) of the Ag/AgCl@$Zn_3V_2O_8$ sample does not show any fluorescence effect. The PL technique can only probe the emissive part, while the energy arising from the recombination between the charge carriers can be released by photons (emissive part) or heat (non-emissive). Therefore, the above PL result suggests that the energy arising from the recombination of electrons and holes may be released in a non-emissive manner [41,45].

The stability of a photocatalyst is another important aspect in practical applications. Fig. 13 shows the RhB-photodegradation performance of the Ag/AgCl@$Zn_3V_2O_8$ (S12 in Table 1) in the recycling use under the visible-light irradiation. It can be seen that its activity reduces slightly after four cycles' RhB-photodegradation reaction, but it still kept at a relatively high level. Eighty percentage of the RhB dye is photodegradated in 30 min, confirming that the Ag/AgCl@$Zn_3V_2O_8$ nanocomposites are relatively stable during the photodegradation process.

To further confirm the active species (h^+, •OH or $\bullet O_2^-$) during the RhB-photodegradation, we designed a series of experiments by introducing different scavengers: H_2O_2 (an

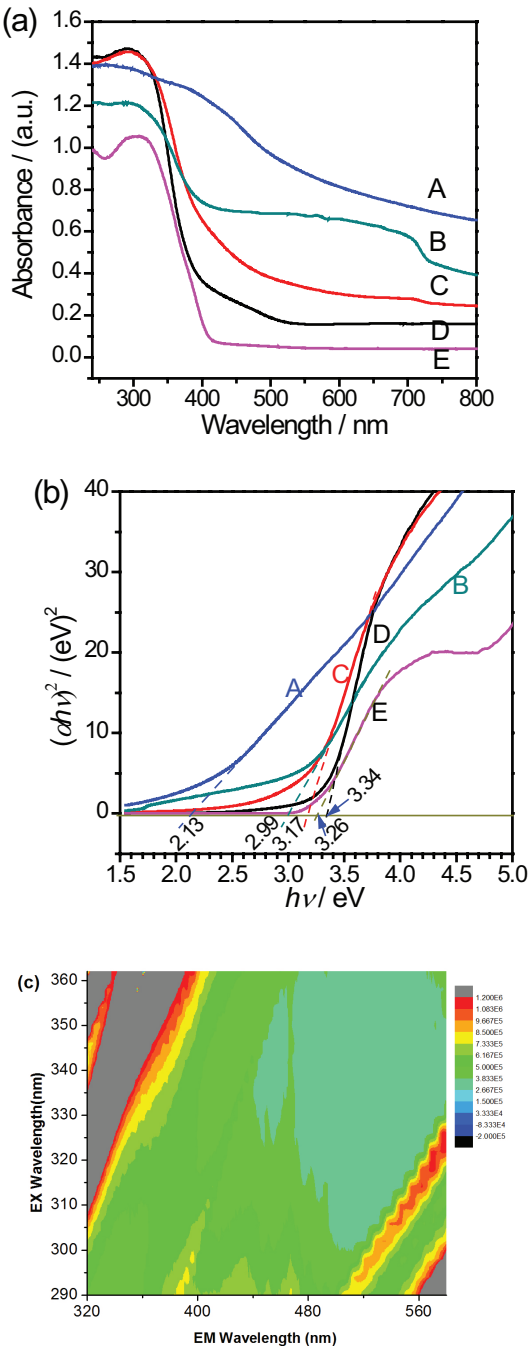

Fig. 12. (a) UV–vis DR spectra and (b) the corresponding plots of $(\alpha h\nu)^2$ vs. photon energy ($h\nu$) of various samples: (A) Ag/AgCl@$Zn_3V_2O_8$ (S12), (B) Ag/AgCl@$Zn_3V_2O_8$ (S14), (C) $Zn_3V_2O_8$ (S15), (D) $Zn_3(OH)_2V_2O_7 \bullet 2H_2O$ and (E) TiO_2 (P25). (c) A 3D photoluminescence (PL) spectrum of Ag/AgCl@$Zn_3V_2O_8$.

electron scavenger) and ethylenediaminetetraacetic acid disodium salt (EDTA-2Na, a hole scavenger) [47]. Fig. 14 shows the typical RhB-photodegradation curves (C/C_0 – t) with or without scavengers. As Figs. 14(a) and (b) show, the photodegradation ability sharply drops when the scavenger of H_2O_2 or EDTA-2Na was introduced. Without any scavenger (Fig. 14(c)), the photodegradation rate constant (k)

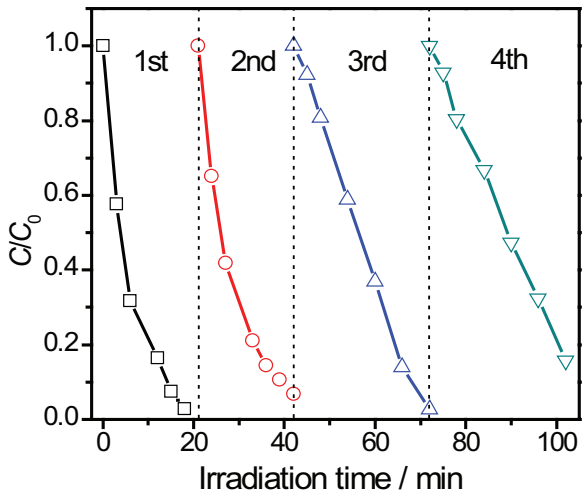

Fig. 13. Recycling use performance of the Ag/AgCl@$Zn_3V_2O_8$ (S12) photocatalyst in photodegradating RhB aqueous solutions under visible-light irradiation ($\lambda > 420$ nm).

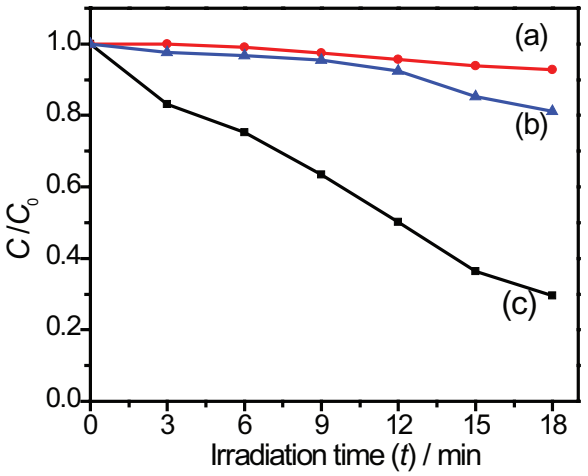

Fig. 14. Influence of various scavengers on photocatalytic RhB degradation with Ag/AgCl@$Zn_3V_2O_8$ nanocomposite as the photocatalyst: (a) H_2O_2, (b) EDTA-2Na and (c) no scavenger.

is 0.04 min^{-1}, whereas the k is 0.004 min^{-1} when the electron (•OH and $•O_2^-$) scavenger (H_2O_2, Fig. 14(a)) is used, and the k is 0.010 min^{-1} in the case of the hole (h^+) scavenger (EDTA-2Na, Fig. 14(b)). Because both electron and hole scavengers depress the RhB-photodegradation activity of the Ag/AgCl@$Zn_3V_2O_8$ nanocomposites, both the electron (•OH and $•O_2^-$) and hole (h^+) in this system are active species in photodegradating RhB dye under the visible-light irradiation. With the support of some similar references [48,49], we can further confirm that $•O_2^-$ and h^+ are the major reactive species in the photocatalytic process. The electron–hole pairs can be separated well in the hierarchical Ag/AgCl@$Zn_3V_2O_8$ photocatalyst, and the efficient electron–hole separation enhances its photocatalytic ability.

Before understanding the photocatalytic mechanism, it is essential to figure out the positions of conduction band (CB) and valence band (VB) of the components in energy bands, based on the following equations [50,51]:

$$E_{CB} = X - E^e - 0.5E_g \quad (5)$$

$$E_{VB} = E_{CB} + E_g \quad (6)$$

where E^e stands for the electron free energy which is about 4.5 eV (vs. hydrogen); X is the electronegativity of the target semiconductor. For the compound of $A_aB_bC_c$, X can be obtained via the following equation [50,51]:

$$X = [x(A)^a x(B)^b x(C)^c]^{1/(a+b+c)} \quad (7)$$

where the $x(I)$ stands for the atomic absolute electronegativity of element I.

For $Zn_3V_2O_8$, the E_g can be determined by its UV–vis DR spectrum (Fig. 12) to be 3.17 eV, $X(Zn_3V_2O_8)$ is calculated to be 5.96 eV according to Eq. (7); so the $E_{CB}(Zn_3V_2O_8) = -0.12$ eV, $E_{VB}(Zn_3V_2O_8) = 3.05$ eV. Similarly, the E_{CB} and E_{VB} of AgCl can be calculated to be –0.06 and 3.19 eV, respectively, according to Eqs. (5)–(7) and the data reported previously [49].

Fig. 15 schematically illustrated the possible mechanism for the photocatalytic degradation of organic pollutants according to the above discussion. As Fig. 15(a) shows, the semiconductors of AgCl and $Zn_3V_2O_8$ can form a tandem heterojunction for charge separation, but their bandgaps are larger than 2.95 eV and the incident visible light in the case of $\lambda \geq 420$ nm cannot be absorbed. Therefore, we thought that the localized surface plasmon resonance (LSPR) effect of Ag species should play a key role in the dye photodegaradation, and the possible degradation mechanism is shown in Fig. 15(b).

First, the metal Ag species absorb visible light due to the LSPR effect, and photogenerated electron–hole pairs under visible-light irradiation (Eq. (8)). The Cl^- ions on the surface of AgCl particles are negatively charged, and the photogenerated holes can transfer to AgCl surface to oxidize Cl^- to Cl^0 atoms, which can oxidize organic pollutants and then regenerate Cl^- ions [43]. In this process, AgCl particles fail to absorb visible light ($\lambda > 420$ nm) and keep stable, due to their large bandgaps (i.e., a direct bandgap of ~5.0 eV and an indirect bandgap of ~3.5 eV). Also, the photogenerated holes can react with OH^- ions to form •OH radicals, which can oxidize organic pollutants. On the other hand, to minimize their active energy, the photogenerated electrons transfer to the CB of the zinc vanadate ($Zn_3V_2O_8$) semiconductor, where these electrons react with O_2 molecules dissolved in the solution and form superoxide ions ($•O_2^-$). Some superoxide ions can undergo a protonation reaction with H_3O^+ ions to generate •OOH radicals, which then react with excess photogenerated electrons to produce H_2O_2, accompanying with the formation of •OH radicals. Various active species, including $•O_2^-$, •OOH, H_2O_2 and •OH, can degradate organic pollutants in the presence of the hierarchical Ag/AgCl@$Zn_3V_2O_8$ photocatalyst [44,45,52]. The possible reactions can be described as Eqs. (9)–(17).

$$Ag + h\nu \rightarrow Ag + h^+ + e^- \quad (8)$$

$$e^- + Zn_3V_2O_8 \rightarrow Zn_3V_2O_8^- \quad (9)$$

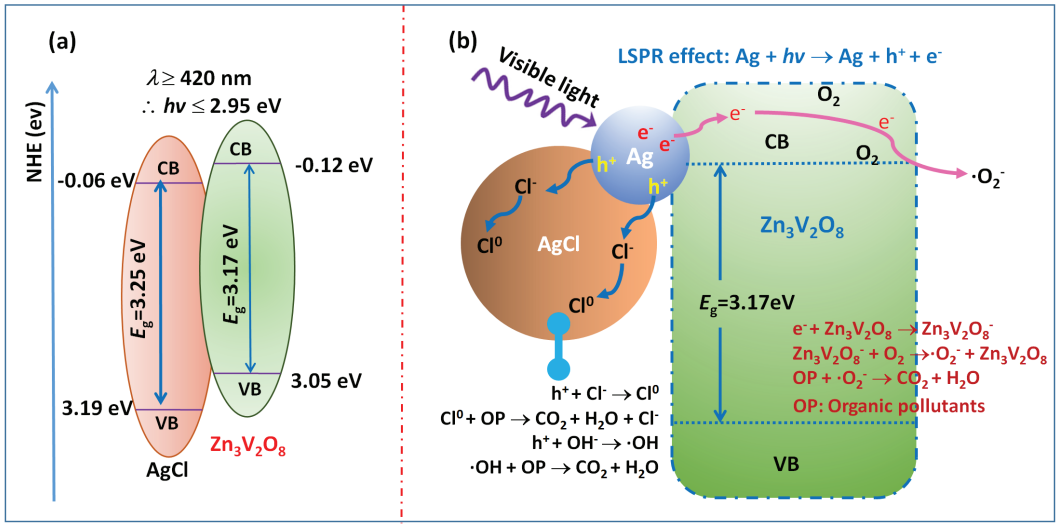

Fig. 15. Schematic mechanism for the visible-light-driven photodegradation of organic pollutants: (a) the AgCl@$Zn_3V_2O_8$ heterojunction and (b) the hierarchical Ag/AgCl@$Zn_3V_2O_8$ nanocomposite.

$$Zn_3V_2O_8^- + O_2 \rightarrow Zn_3V_2O_8 + \bullet O_2^- \quad (10)$$

$$\bullet O_2^- + H_3O^+ \rightarrow \bullet OOH + H_2O \quad (11)$$

$$\bullet OOH + Zn_3V_2O_8^- + H_3O^+ \rightarrow H_2O_2 + Zn_3V_2O_8 \quad (12)$$

$$H_2O_2 + Zn_3V_2O_8^- \rightarrow \bullet OH + OH^- + Zn_3V_2O_8 \quad (13)$$

$$h^+ + Cl^- \rightarrow Cl^0 \quad (14)$$

$$h^+ + OH^- \rightarrow \bullet OH \quad (15)$$

$$Cl^0 + OP \rightarrow CO_2 + H_2O + Cl^- \quad (16)$$

$$\bullet O_2^-/\bullet OH + OP \rightarrow CO_2 + H_2O \quad (\text{OP: Organic pollutants}) \quad (17)$$

4. Conclusions

Two-dimensional $Zn_3V_2O_8$ nanoplates (~10 nm in thickness) were synthesized by topochemically transforming flower-like $Zn_3(OH)_2V_2O_7 \bullet 2H_2O$ spheres at 300°C–450°C in air, and the as-obtained $Zn_3V_2O_8$ nanoplates were then used as substrates to construct hierarchical Ag/AgCl@$Zn_3V_2O_8$ nanocomposites via an in situ growth process. The Ag/AgCl@$Zn_3V_2O_8$ nanocomposites obtained under optimum conditions ($R_{Ag/Zn}$ = ~0.23, photoreduction time = 1 min, calcination temperature = 400°C) are of highly enhanced efficient performance in photodegradating RhB dye and isopropanol under the visible-light irradiation. The efficient separation of active species (h^+, •OH and $\bullet O_2^-$) and high absorption of visible light are the key reasons for enhancing their photocatalytic performance. This work provides an alternative strategy to design and synthesize high-performance visible-light-driven photocatalysts for environmental applications.

Acknowledgments

This work was partly sponsored by National Natural Science Foundation of China (51574205, 51172211), China Postdoctoral Science Foundation (2013M531682, 2014T70682), Program for Science and Technology Innovation Talents in Universities of Henan Province (14HASTIT011), Special Support Program for High-End Talents of Zhengzhou University (ZDGD13001), Plan for Scientific Innovation Talent of Henan Province (154100510003), and Dongguan University of Technology (G200906-17).

References

[1] T. Hisatomi, J. Kubota, K. Domen, Recent advances in semiconductors for photocatalytic and photoelectrochemical water splitting, Chem. Soc. Rev., 43 (2014) 7520–7535.
[2] A. Kubacka, M.F. García, G. Colón, Advanced nanoarchitectures for solar photocatalytic applications, Chem. Rev., 112 (2012) 1555–1614.
[3] M.L. Marin, L.S. Juanes, A. Arques, A.M. Amat, M.A. Miranda, Organic photocatalysts for the oxidation of pollutants and model compounds, Chem. Rev., 112 (2012) 1710–1750.
[4] J.C. Colmenares, R. Luque, Heterogeneous photocatalytic nanomaterials: prospects and challenges in selective transformations of biomass-derived compounds, Chem. Soc. Rev., 43 (2014) 765–778.
[5] J. Schneider, M. Matsuoka, M. Takeuchi, J. Zhang, Y. Horiuchi, M. Anpo, D.W. Bahnemann, Understanding TiO_2 photocatalysis: mechanisms and materials, Chem. Rev., 114 (2014) 9919–9986.
[6] R. Asahi, T. Morikawa, H. Irie, T. Ohwaki, Nitrogen-doped titanium dioxide as visible-light-sensitive photocatalyst: designs, developments, and prospects, Chem. Rev., 114 (2014) 9824–9852.
[7] Y. Ma, X. Wang, Y. Jia, X. Chen, H. Han, C. Li, Titanium dioxide-based nanomaterials for photocatalytic fuel generations, Chem. Rev., 114 (2014) 9987–10043.
[8] D. Venieri, I. Gounaki, V. Binas, A. Zachopoulos, G. Kiriakidis, D. Mantzavinos, Inactivation of MS_2 coliphage in sewage by solar photocatalysis using metal-doped TiO_2, Appl. Catal., B, 178 (2015) 54–64.
[9] Z. Zhao, Y. Wang, J. Xu, C. Shang, Y. Wang, AgCl-loaded mesoporous anatase TiO_2 with large specific surface area for enhancing photocatalysis, Appl. Surf. Sci., 351 (2015) 416–424.

[10] Z. Zhang, W. Wang, E. Gao, S. Sun, L. Zhang, Photocatalysis coupled with thermal effect induced by SPR on Ag-loaded Bi_2WO_6 with enhanced photocatalytic activity, J. Phys. Chem. C, 116 (2012) 25898–25903.
[11] Y. Luo, G. Tan, G. Dong, H. Ren, A. Xia, Effects of structure, morphology, and up-conversion on Nd-doped $BiVO_4$ system with high photocatalytic activity, Ceram. Int., 41 (2015) 3259–3268.
[12] J. Bae, J.B. Han, X.M. Zhang, M. Wei, X. Duan, Y. Zhang, Z.L. Wang, ZnO nanotubes grown at low temperature using Ga as catalysts and their enhanced photocatalytic activities, J. Phys. Chem. C, 113 (2009) 10379–10383.
[13] Z. Zhang, L. Zhang, M.N. Hedhili, H. Zhang, P. Wang, Plasmonic gold nanocrystals coupled with photonic crystal seamlessly on TiO_2 nanotube photoelectrodes for efficient visible light photoelectrochemical water splitting, Nano Lett., 13 (2013) 14–20.
[14] N. Kumar, V.K. Komarala, V. Dutta, In-situ synthesis of Au–CdS plasmonic photocatalyst by continuous spray pyrolysis and its visible light photocatalysis, Chem. Eur. J., 236 (2014) 66–74.
[15] B.H. Nguyen, V.H. Nguyen, Recent advances in research on plasmonic enhancement of photocatalysis, Adv. Nat. Sci.: Nanosci. Nanotechnol., 6 (2015) 043001.
[16] L. Touahir, A.T. Jenkins, R. Boukherroub, A.C. Gouget-Laemmel, J.N. Chazalviel, J. Peretti, F. Ozanam, S. Szunerits, Surface plasmon-enhanced fluorescence spectroscopy on silver based SPR substrates, J. Phys. Chem. C, 114 (2010) 22582–22589.
[17] J. Shu, Z. Wang, G. Xia, Y. Zheng, L. Yang, W. Zhang, One-pot synthesis of AgCl@Ag hybrid photocatalyst with high photocatalytic activity and photostability under visible light and sunlight irradiation, Chem. Eur. J., 252 (2014) 374–381.
[18] P. Wang, B. Huang, X. Qin, X. Zhang, Y. Dai, J. Wei, M.H. Whangbo, Ag@AgCl: a highly efficient and stable photocatalyst active under visible light, Angew. Chem. Int. Ed., 47 (2008) 7931–7933.
[19] Y. Tang, Z. Jiang, G. Xing, A. Li, P.D. Kanhere, Y. Zhang, T.C. Sum, S. Li, X. Chen, Z. Dong, Efficient Ag@AgCl cubic cage photocatalysts profit from ultrafast plasmon-induced electron transfer processes, Adv. Funct. Mater., 23 (2013) 2932–2940.
[20] R. Dong, B. Tian, C. Zeng, T. Li, T. Wang, J. Zhang, Ecofriendly synthesis and photocatalytic activity of uniform cubic Ag@AgCl plasmonic photocatalyst, J. Phys. Chem. C, 117 (2013) 213–220.
[21] P. Wang, B. Huang, Z. Lou, X. Zhang, X. Qin, Y. Dai, Z. Zheng, X. Wang, Synthesis of highly efficient Ag@AgCl plasmonic photocatalysts with various structures, Chem. Eur. J., 16 (2010) 538–544.
[22] G. Jiang, X. Li, Z. Wei, T. Jiang, X. Du, W. Chen, Growth of N-doped BiOBr nanosheets on carbon fibers for photocatalytic degradation of organic pollutants under visible light irradiation, Powder Technol. 260 (2014) 84–89.
[23] G. Jiang, Z. Wei, H. Chen, X. Du, L. Li, Y. Liu, Q. Huang, W. Chen, Preparation of novel carbon nanofibers with BiOBr and AgBr decoration for the photocatalytic degradation of rhodamine B, RSC Adv., 5 (2015) 30433–30437.
[24] Z. Wei, G. Jiang, L. Shen, X. Li, X. Wang, W. Chen, Preparation of Mn-doped BiOBr microspheres for efficient visible-light-induced photocatalysis, MRS Commun., 3 (2013) 145–149.
[25] J. Low, J. Yu, Q. Li, B. Cheng, Enhanced visible-light photocatalytic activity of plasmonic Ag and graphene co-modified Bi_2WO_6 nanosheets, Phys. Chem. Chem. Phys., 16 (2014) 1111–1120.
[26] G. Jiang, X. Wang, Z. Wei, X. Li, X. Xi, R. Hu, B. Tang, R. Wang, S. Wang, T. Wang, W. Chen, Photocatalytic properties of hierarchical structures based on Fe-doped BiOBr hollow microspheres, J. Mater. Chem. A, 1 (2013) 2406–2410.
[27] D. Chen, T. Li, Q. Chen, J. Gao, J. Li, X. Li, R. Zhang, J. Sun, L. Gao, Hierarchically plasmonic photocatalysts of Ag/AgCl nanocrystals coupled with single-crystalline WO_3 nanoplates, Nanoscale, 4 (2012) 5431–5439.
[28] S. Zhang, J. Li, X. Wang, Y. Huang, M. Zeng, J. Xu, In situ ion exchange synthesis of strongly coupled Ag@AgCl/g-C_3N_4 porous nanosheets as plasmonic photocatalyst for highly efficient visible-light photocatalysis, ACS Appl. Mater. Interfaces, 6 (2014) 22116–22125.
[29] W.J. Ong, L.K. Putri, L.L. Tan, S.P. Chai, S.T. Yong, Heterostructured AgX/g-C_3N_4 (X = Cl and Br) nanocomposites via a sonication-assisted deposition-precipitation approach: emerging role of halide ions in the synergistic photocatalytic reduction of carbon dioxide, Appl. Catal., B, 180 (2016) 530–543.
[30] H.A. Zadeh, E. Rahimpour, Utilizing of Ag@AgCl@graphene oxide@Fe_3O_4 nanocomposite as a magnetic plasmonic nanophotocatalyst in light-initiated H_2O_2 generation and chemiluminescence detection of nitrite, Talanta, 144 (2015) 769–777.
[31] H. Li, Y. Sun, B. Cai, S. Gan, D. Han, L, Niu, T, Wu, Hierarchically Z-scheme photocatalyst of Ag@AgCl decorated on $BiVO_4$ (040) with enhancing photoelectrochemical and photocatalytic performance, Appl. Catal., B, 170–171 (2015) 206–214.
[32] R. Wang, G. Jiang, X. Wang, R. Hu, X. Xi, S. Bao, Y. Zhou, T. Tong, S. Wang, T. Wang, W. Chen, Efficient visible-light-induced photocatalytic activity over the novel Ti-doped BiOBr microspheres, Powder Technol., 228 (2012) 258–263.
[33] T. Xiong, H. Zhang, Y. Zhang, F. Dong, Ternary Ag/AgCl/$BiOIO_3$ composites for enhanced visible-light-driven photocatalysis, Chin. J. Catal., 36 (2015) 2155–2163.
[34] S.Y. Zhang, X. Xiao, M. Lu, Z.Q. Li, $Zn_3V_2O_7(OH)_2{\cdot}2H_2O$ and $Zn_3(VO_4)_2$ 3D microspheres as anode materials for lithium-ion batteries, J. Mater. Sci., 48 (2013) 3679–3685.
[35] F. Wang, W. Wu, X. Sun, S. Song, Y. Xing, J. Wang, D. Yu, Z. Su, Synthesis of hexagonal $Zn_3(OH)_2V_2O_7{\cdot}2H_2O$ nanoplates by a hydrothermal approach: magnetic and photocatalytic properties, Mater. Charact., 86 (2013) 139–145.
[36] R. Shi, Y. Wang, F. Zhou, Y. Zhu, $Zn_3V_2O_7(OH)_2(H_2O)_2$ and $Zn_3V_2O_8$ nanostructures: controlled fabrication and photocatalytic performance, J. Mater. Chem., 21 (2011) 6313–6320.
[37] D. Chen, M. Liu, Q. Chen, L. Ge, B. Fan, H. Wang, H. Lu, D. Yang, R. Zhang, Q. Yan, G. Shao, J. Sun, L. Gao, Large-scale synthesis and enhanced visible-light-driven photocatalytic performance of hierarchical Ag/AgCl nanocrystals derived from freeze-dried PVP–Ag^+ hybrid precursors with porosity, Appl. Catal., B, 144 (2014) 394–407.
[38] G. Jiang, R. Wang, X. Wang, X. Xi, R. Hu, Y. Zhou, S. Wang, T. Wang, W. Chen, Novel highly active visible-light-induced photocatalysts based on BiOBr with Ti doping and Ag decorating, ACS Appl. Mater. Interfaces,4 (2012) 4440–4444.
[39] Q. Wang, L. Zheng, Y. Bai, J. Zhao, F. Wang, R. Zhang, H. Huang, B. Su, $Zn_3(OH)_2V_2O_7{\cdot}2H_2O$/g-$C_3N_4$: a novel composite for efficient photodegradation of methylene blue under visible-light irradiation, Appl. Surf. Sci., 347 (2015) 602–609.
[40] K.S. Sing, D.H. Everett, R.A. Haul, L. Moscou, R.A. Pierotti, J. Rouquerol, T. Siemieniewska, Reporting physisorption data for gas/solid systems with special reference to the determination of surface area and porosity, Pure Appl. Chem., 57 (1985) 603–619.
[41] L. Li, Y. Yang, X. Liu, R. Fan, Y. Shi, S. Li, L. Zhang, F. Xiao, P. Tang, R. Xu, W. Zhang, Y. Wang, L. Ma, A direct synthesis of B-doped TiO_2 and its photocatalytic performance on degradation of RhB, Appl. Surf. Sci., 265 (2013) 36–40.
[42] C. Mondal, M. Gunguly, A.K. SinhaSong, J. Pal, R. Sahoo, T. Pal, Robust cubooctahedron $Zn_3V_2O_8$ in gram quantity: a material for photocatalytic dye degradation in water, CrystEngComm, 15 (2013) 6745–6751.
[43] H. Daupor, S. Wongnawa, Urchinlike Ag/AgCl photocatalyst: synthesis, characterization, and activity, Appl. Catal., A, 473 (2014) 59–69.
[44] J. Yu, G. Dai, B. Huang, Fabrication and characterization of visible-light-driven plasmonic photocatalyst Ag/AgCl/TiO_2 nanotube arrays, J. Phys. Chem. C, 113 (2009) 16394–16401.
[45] Y. Tian, T. Tatsuma, Mechanisms and applications of plasmon-induced charge separation at TiO_2 films loaded with gold nanoparticles, J. Am. Chem. Soc., 127 (2005) 7632–7637.
[46] H.Y. Aziz, S.Y. Maryam, Fe_3O_4/ZnO/Ag_3VO_4/AgI nanocomposites: quaternary magnetic photocatalysts with excellent activity in degradation of water pollutants under visible light, Sep. Purif. Methods, 166 (2016) 63–72.

[47] D.L. Chen, S.H. Yoo, Q. Huang, G. Ali, S.O. Cho, Sonochemical synthesis of Ag/AgCl nanocubes and their efficient visible-light-driven photocatalytic performance, Chem. Eur. J., 18 (2012) 5192–5200.
[48] D.F. Wang, Z.G. Zhou, J.H. Ye, Photocatalytic O_2 evolution with the visible-light-driven photocatalysts $M_3V_2O_8$ (M = Mg, Zn), Res. Chem. Intermed., 31(2005) 433–439.
[49] Y.Q. Yang, G.K. Zhang, W. Xu, Facile synthesis and photocatalytic properties of Ag-AgCl-TiO_2/rectorite composite, J. Colloid Interface Sci., 376 (2012) 217–223.
[50] M. Mitra, H.Y. Aziz, A. Masoud, Fabrication of novel magnetically separable nanocomposites using graphitic carbon nitride, silver phosphate and silver chloride and their applications in photocatalytic removal of different pollutants using visible-light irradiation, J. Colloid Interface Sci., 480 (2016) 218–231.
[51] M. Mitra, H.Y. Aziz, Magnetically separable ternary g-C_3N_4/Fe_3O_4/BiOI nanocomposites: novel visible-light-driven photocatalysts based on graphitic carbon nitride, J. Colloid Interface Sci., 465 (2016) 83–92.
[52] S.G. Maryam, H.Y. Aziz, Novel magnetically separable ZnO/AgBr/Fe_3O_4/Ag_3VO_4 nanocomposites with tandem n-n heterojunctions as highly efficient visible-light-driven photocatalysts, RSC Adv., 6 (2016) 2402–2413.